

DLP-Printable Porous Cryogels for 3D Soft Tactile Sensing

*Original*

DLP-Printable Porous Cryogels for 3D Soft Tactile Sensing / Cafiso, D.; Bernabei, F.; Lo Preti, M.; Lantean, S.; Roppolo, I.; Pirri, C. F.; Beccai, L.. - In: ADVANCED MATERIALS TECHNOLOGIES. - ISSN 2365-709X. - (2024).  
[10.1002/admt.202302041]

*Availability:*

This version is available at: 11583/2987733 since: 2024-04-11T10:50:38Z

*Publisher:*

Wiley

*Published*

DOI:10.1002/admt.202302041

*Terms of use:*

This article is made available under terms and conditions as specified in the corresponding bibliographic description in the repository

*Publisher copyright*

(Article begins on next page)

# DLP-Printable Porous Cryogels for 3D Soft Tactile Sensing

Diana Cafiso,\* Federico Bernabei, Matteo Lo Preti, Simone Lantean, Ignazio Roppolo, Candido Fabrizio Pirri, and Lucia Beccai\*

Three-Dimensional (3D) printed porous materials hold the potential for various soft sensing applications due to their remarkable flexibility, low density, and customizable geometries. However, developing versatile and efficient fabrication methods is crucial to unlock their full potential. A novel approach is introduced by combining Digital Light Processing (DLP) 3D printing and freeze-drying to manufacture deformable cryogels featuring intricate morphologies. Photocurable hydrogels based on Poly(3,4-ethylenedioxythiophene)Polystyrene sulfonate (PEDOT:PSS), Polyethylene glycol Diacrylate (PEGDA) and Ethylene Glycol (EG) are successfully printed and lyophilized. In this way, porous cryogels with tailorable properties are achieved. Microporosity varies from 68% to 96%, according to the chemical composition. Ultra-soft cryogels with a compressive modulus of 0.13 MPa are fabricated by adding a reactive diluent. As a result of the cryogelation process, which effectively removes water from the hydrogels, microporous structures with details as fine as 100  $\mu\text{m}$  are obtained. The achieved freedom of design is exploited to fabricate resistive force sensors with a honeycomb lattice morphology. The sensitivity and the working range of the sensors can be tailored by tuning the size of the cells, paving the way for sensors with programmable architectures that can meet diverse requirements.

## 1. Introduction

The rapid progress of soft robotics demands for highly versatile soft sensors for the detection of mechanical stimuli, coming from the outside world or from the robot itself,<sup>[1]</sup> which can fulfill different requirements in order to address new challenges.<sup>[2–5]</sup> Consequently, there has been a surge in the research on novel materials and smart technologies to enable the efficient and tunable fabrication of soft sensors with arbitrary architectures, sizes, and configurations. Within this context, Three-Dimensional (3D) printing has emerged as a robust tool for tailoring the properties and engineering the structure of soft sensors.<sup>[6]</sup> It enabled the creation of sensors capable of multi-stimuli detection<sup>[7]</sup> tunable piezoresistivity,<sup>[8]</sup> micro strain gauge with micro-newton sensing resolution,<sup>[9]</sup> and integrated systems coupling sensing and actuation in a seamless process.<sup>[10]</sup>

Among the various 3D printing technologies, vat photopolymerization stands

out for its ability to construct components with highly complex geometries and fine resolution.<sup>[11]</sup> Specifically, Digital Light Processing (DLP) has been utilized to fabricate soft sensors due to its advantages in terms of faster building speed, high shape fidelity, and excellent resolution. Over time, DLP-printed soft mechanical sensors were developed using various materials, including hydrogels.<sup>[12,13]</sup>

Hydrogels are 3D polymeric networks that contain water within their porous structure.<sup>[14,15]</sup> The chemical composition of the hydrogels can be tailored to meet different requirements, such as high transparency,<sup>[16]</sup> inherent softness,<sup>[17]</sup> biocompatibility,<sup>[18]</sup> and self-healing ability.<sup>[19]</sup> These features have been increasingly exploited in soft sensing, especially in the field of wearable electronics.<sup>[20]</sup> This growing knowledge has been leveraged in the field of soft robotics to obtain hydrogel-based sensors with diverse mechanical, electrical, functional, and morphological properties. Over the years, a wide range of hydrogel systems has been investigated, exploring different polymers, synthesis' approaches, solvents, fillers, and various parameters such as the ratio between liquid and solid phases and the polymerization rate.<sup>[21]</sup> The electrical conductivity of these hydrogels is usually given by conductive nanofillers,<sup>[22]</sup> salts,<sup>[23,24]</sup> or conductive polymers, such as Poly(3,4-ethylenedioxythiophene) Polystyrene sulfonate (PEDOT:PSS).<sup>[25]</sup> In particular, the latter

D. Cafiso, F. Bernabei, M. Lo Preti, S. Lantean, L. Beccai  
Soft BioRobotics Perception Lab  
Istituto Italiano di Tecnologia  
Via Morego 30, Genova 16163, Italy  
E-mail: [diana.cafiso@iit.it](mailto:diana.cafiso@iit.it); [lucia.beccai@iit.it](mailto:lucia.beccai@iit.it)

D. Cafiso, I. Roppolo, C. F. Pirri  
Department of Applied Science and Technology  
Politecnico di Torino  
C.so Duca degli Abruzzi 24, Turin 10129, Italy

F. Bernabei  
The BioRobotics Institute  
Scuola Superiore Sant'Anna  
Viale Rinaldo Piaggio 34, Pontedera 56025, Italy

I. Roppolo, C. F. Pirri  
Center for Sustainable Future Technologies @Polito  
Istituto Italiano di Tecnologia  
Via Livorno, 60, Turin 10144, Italy

The ORCID identification number(s) for the author(s) of this article can be found under <https://doi.org/10.1002/admt.202302041>

© 2024 The Authors. Advanced Materials Technologies published by Wiley-VCH GmbH. This is an open access article under the terms of the Creative Commons Attribution-NonCommercial-NoDerivs License, which permits use and distribution in any medium, provided the original work is properly cited, the use is non-commercial and no modifications or adaptations are made.

DOI: 10.1002/admt.202302041

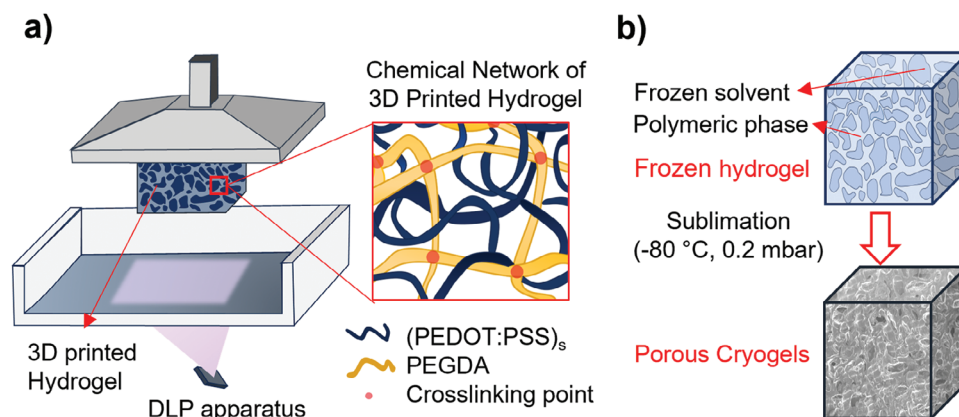


**Figure 1.** Scheme of the fabrication protocol for the 3D porous cryogels. a) The hydrogels were 3D-printed via DLP. During the printing, the formation of chemical cross-links between the polymer chains resulted in the formation of cured hydrogels. b) The printed hydrogels were frozen and then lyophilized in order to remove the ice crystals and form porous, dehydrated cryogels.

has been widely explored due to its bio-compatibility, tailorable electrical properties and stability to air and moisture.<sup>[26]</sup>

However, despite the fascinating properties of hydrogel sensors, some limitations remain for reliable sensing applications, mainly related to the low durability caused by the solvent's evaporation, which modifies the hydrogel's size and deteriorate its mechanical and electrical properties.<sup>[27]</sup> This is particularly important for pressure and force sensors, whose transducers, which are solicited mechanically in a repeated manner, must reliably convert the mechanical input into an electrical output.

Porous materials have also piqued the interest of researchers in soft sensing due to their promising electrical and mechanical properties. The presence of pores enables the alteration of conductive paths within the cells during the loading phase, while it increases the material's deformability leading to higher sensitivities.<sup>[28]</sup> Various methods, such as chemical etching,<sup>[29]</sup> emulsions,<sup>[30,31]</sup> and particle templating,<sup>[32,33]</sup> have been utilized to fabricate porous sensors.

A low-cost and feasible method to introduce porosity involves the removal of the solvent from hydrogels. Hydrogels can be dried in various ways under different temperatures and pressure conditions. Among them, freeze-drying is a simple and cost-effective technique that limits the collapse of the pores and structure, resulting in the formation of a cryogel.<sup>[34]</sup> The term "cryogelation" is used herein to refer to the process involving the polymerization of the hydrogel, freezing the sample, removing ice crystals through freeze-drying and thawing, to obtain a porous material without any liquid phase. To the best of our knowledge, there are only a few works on soft sensors based on 3D printed cryogels.<sup>[35–38]</sup> Notably, these sensors were manufactured via direct ink writing, which, however, can limit both the design's degrees of freedom and the printing accuracy, compared to photopolymerization-based 3D printing.<sup>[39]</sup> Notably, no examples of 3D soft sensors obtained by combining DLP additive manufacturing and cryogelation have been reported so far.

In this study, we present a simple and tunable fabrication approach for soft porous sensors with 3D-printed architectures. Light-curable hydrogels were synthesized by combining Poly(ethylene glycol) diacrylate (PEGDA) and PEDOT:PSS. The ratio between these two components was carefully designed to

achieve a compromise between mechanical and electrical properties. The resulting hydrogel was then 3D printed using DLP technology, allowing the creation of complex shapes with high resolution and shape fidelity. This enabled exploring the feasibility of customizable conductive structures. As a proof of concept, soft force sensors with honeycomb morphology having different dimensions were fabricated and evaluated.

## 2. Results

**Figure 1** shows the fabrication of the conductive cryogels. For the synthesis of the precursors' hydrogels, the pre-polymer PEGDA was selected as the hydrogel's backbone due to its strong hydrophilicity and fast reaction kinetics under UV light, which is related to its acrylate groups.<sup>[40,41]</sup> The photocurable monomer PEGDA and the photoinitiator Lithium phenyl-2,4,6-trimethylbenzoylphosphine (LAP) were dissolved in a water-based solution of PEDOT:PSS, ((PEDOT:PSS)s). Both PEGDA and LAP, being hydrophilic, exhibited good solubility in ((PEDOT:PSS)s).

### 2.1. Material Study

The adsorption profiles of the formulations were determined by Ultraviolet-Visible (UV-Vis) spectroscopy and reported in **Figure 2a**. All the compositions absorbed light in the working range of the DLP, i.e., 385 – 405 nm, confirming their suitability for printing. The samples with larger fractions of PEGDA showed a higher absorbance at these wavelengths due to the higher amount of the photoinitiator, which exhibited a broad absorbance between 350 nm and 420 nm, with a peak at 380 nm.<sup>[42]</sup> The pristine ((PEDOT:PSS)s) had higher absorbance than PEGDA in the range of interest, which may compete with the absorption of LAP in the formulation with larger amounts of ((PEDOT:PSS)s). The formulation reaction to UV exposure was investigated through real-time photo-rheology analysis. The experiments were performed at a strain amplitude of 0.1%, at which all the compositions were within the range of the linear viscoelastic

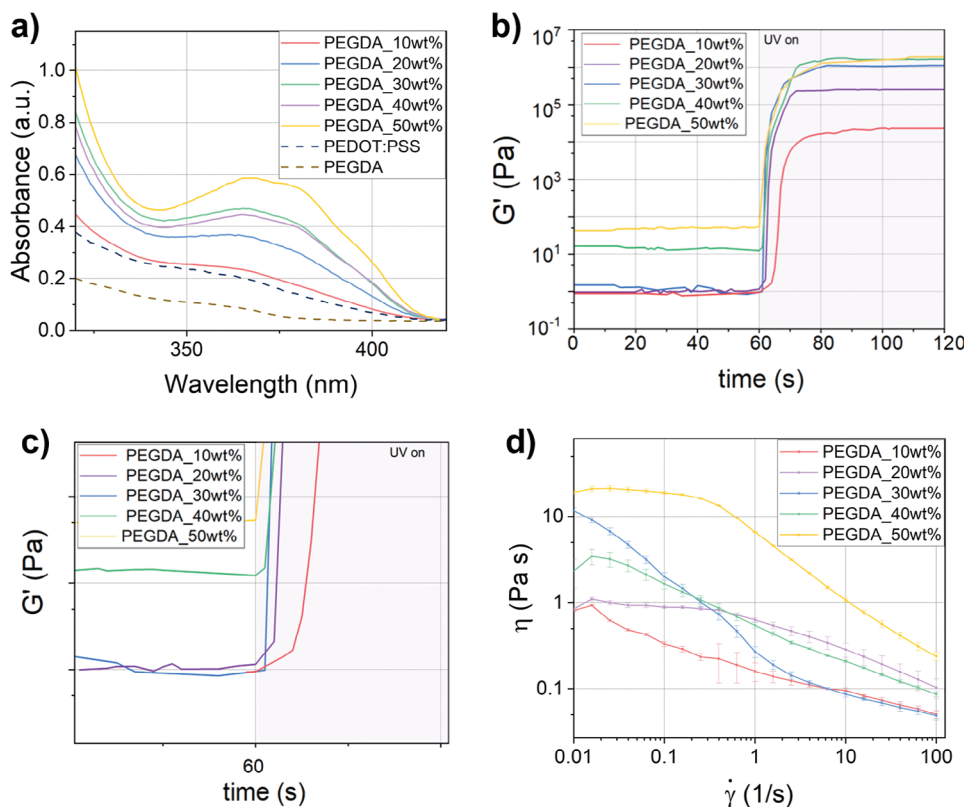


**Figure 2.** a) Absorbance spectra of the formulations and of PEGDA and pedotpss solutions in the wavelength range working of DLP. b) Real-time photorheology of the hydrogels with different chemical composition. The storage moduli  $G'$  is plotted against time. The UV lamp was switched on after 60s. c) Magnification of the photorheology results at 60s to observe the onset of polymerization. d) Viscosity  $\eta$  of the formulations at increasing shear rate values.

region (see Figure S1a, Supporting Information). Then, the variation of the storage modulus  $G'$  of the formulations under UV exposure was measured over time, as shown in Figure 2b. The  $G'$  value after photopolymerization increased together with the increase of PEGDA in the formulation. This was expected since a higher cross-linker content led to tighter and more rigid networks. Furthermore, the onset of the reaction occurred earlier when the amount of PEGDA increased (Figure 2c). This is again related to the amount of reactive groups in the formulations and, accordingly, the polymerization of the samples containing only the 10 wt% of PEGDA resulted considerably slower than the others. Nevertheless, the reaction was completed within 20s, which is an acceptable value to ensure short DLP printing times. All the compositions exhibited a suitable viscosity for the DLP printing (inferior to 5 Pa s at a shear rate of  $30 \text{ s}^{-1}$  [43]), with the viscosity decreasing for lower amounts of PEGDA (Figure 2d). These results were used as preliminary information for printability tests. All the formulations resulted printable via DLP, with shorter exposure times needed for the samples with higher content of PEGDA, in good agreement with photorheology results (see Table S1, Supporting Information).

Simple cubic-shape specimens were 3D printed to assess their electrical conductivity (Figure S1b, Supporting Information). As the amount of PEDOT:PSS increased, the resistivity of the samples decreased from 80 kΩ cm to a few kΩ cm, and the electrical conductivity increased accordingly. The high resistivity of the

material could be attributed to the specific morphology of PEDOT:PSS complexes in water, which consists of an electrically conductive core of PEDOT-coiled chains surrounded by a shell of hydrophilic, insulating PSS molecules. The shell-core morphology and the existence of PSS un-complexed molecules reduce the carrier mobility of the overall material. [44] Several polar solvents can be used to enhance the electrical conductivity of pedotpss, such as N,N-Dimethylformamide, [45] sorbitol, [46] dimethyl sulfoxide [47] and Ethylene Glycol (EG). [48] In this study, the most conductive formulation (PEGDA equal to 10 wt%) was modified with different amounts of EG. The concentration of PEGDA was fixed at 10 wt% and the EG/(PEDOT:PSS)s ratio was varied to determine the optimal amount of the dopant. Notably, the solvent significantly improved the electrical conductivity. As shown in Figure S1c,d (Supporting Information), the resistivity decreased by two orders of magnitude, likely due to the formation of hydrogen bonds between EG and PSS molecules, which caused the separation of PSS from PEDOT chains and resulted in the linear orientation of PEDOT chains. [49] This enhanced the electrical conductivity. Above EG/(PEDOT:PSS)s = 8 wt%, no significant decrease of resistivity was observed. Therefore, this ratio was selected for fabricating hydrogel samples with increasing amounts of PEGDA to assess the morphology of the cryogels with different chemical compositions.

Therefore, formulations containing from 10% wt to 50% wt of PEGDA, and EG, (referred as P10, P20, P30, P40, and P50), were

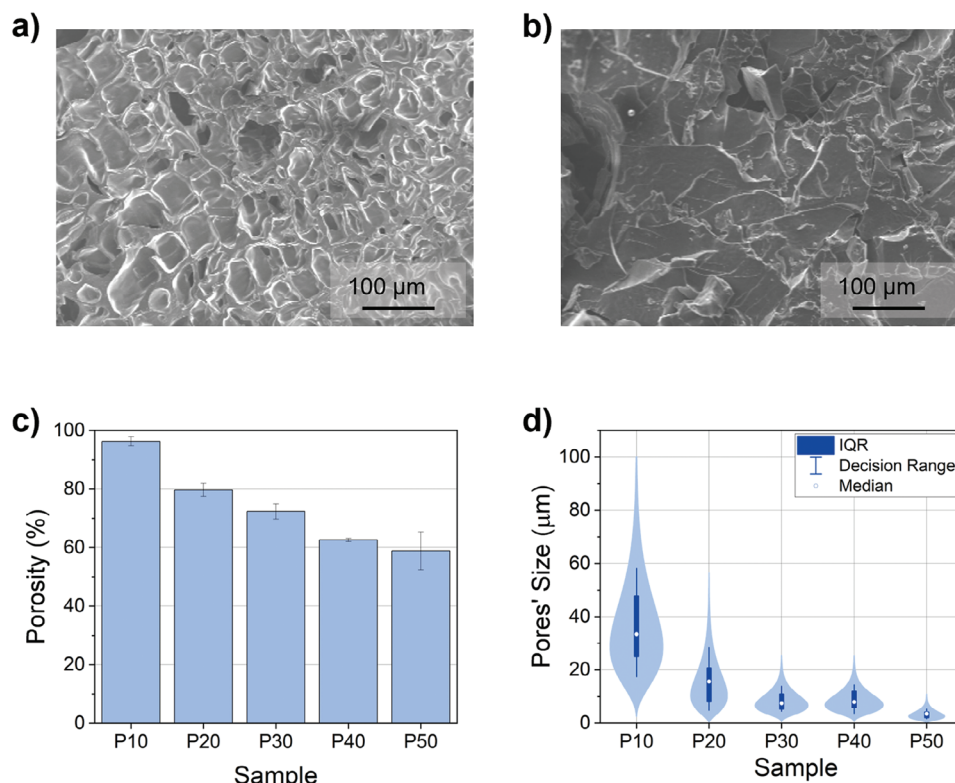


**Figure 3.** SEM images of the cryogels with: a) 10 wt% of PEGDA, showing a microporous morphology; and, b) 50 wt% of PEGDA, which possessed a more dense network. c) Total Porosity (P) of the cryogels according to their chemical compositions. d) Violin plots representing the statistical distribution of the pores' size for the cryogels, reporting the median value, the decision range for the outliers and the interquartile range (IQR).

3D printed in cubic samples and subsequently lyophilized to fabricate the corresponding cryogels. The lyophilization process, as depicted in Figure 1b, involved freezing the samples, followed by depressurization to remove the ice crystals through sublimation. This method effectively eliminated the water of the conductive hydrogels, preventing the collapse due to capillary pressure during atmospheric drying and maintaining the original appearance of the samples. Regarding the EG, the Thermogravimetric Analysis (TGA) and the Differential Thermal Analysis (DTA) thermograms of doped and undoped P10 cryogels were analyzed to determine whether residual remained in the samples after freeze-drying. As reported in Figure S1e (Supporting Information), the P10 doped cryogels showed a weight decrease of 10% between 50 and 200 °C, while the undoped ones had a loss of only 2.5%. This weight loss is compatible with the evaporation of the initial 7% of EG (boiling point 195 °C, also coherent with the first peak present in DTA in Figure S1f, Supporting Information), which consequently remained trapped in the polymeric network after the freeze-drying step. The porous morphology of the cryogels was confirmed by Scanning Electron Microscope (SEM) analysis (Figure 3a,b). Similarly to other porous materials obtained via freeze-drying,<sup>[50,51]</sup> the samples' inner sections appear more porous than the external surfaces (Figure S2, Supporting Information). It should be noted that formulations P50, P40, P30, and P20 exhibited the occurrence of internal cracks, especially at the interface between the 3D printed layers, and formations of debris (see Figure S3, Supporting Information), due

to the growth of ice crystals during the cooling phase.<sup>[52]</sup> Nevertheless, this aspect, which is a common drawback of freeze-drying with respect to other drying methods such as supercritical drying,<sup>[53]</sup> was not observed for the cryogels with lower amounts of PEGDA. The different cryogels showed micro-pores with various geometries, then, their size was evaluated by means of the maximum Feret Diameter, i.e., the longest distance between two points along the pore's boundary.<sup>[54]</sup> The microstructure of the cryogels, in terms of total porosity and pores' size, was found to be influenced by the total concentration of PEGDA. In fact, the total porosity increased by decreasing the amount of PEGDA, as highlighted in Figure 3c. Figure 3d reports the distributions of cryogels' pores' size as violin plots. All the distributions were asymmetric and could be fitted with a Gamma distribution,<sup>[55]</sup> as reported in the Table S2 (Supporting Information), with the P10 cryogels showing a tail toward larger pores and the highest median value among the samples. In particular, by reducing the amount of PEGDA from 50 to 10 wt%, the median value of the pores increased from 3.44 to 37 μm, proving that low-dense cryogels with larger pores could be fabricated by minimizing the amount of PEGDA. The solid concentration and porosity played a key role in the mechanical properties of the cryogels, as demonstrated in Figure 4a. Samples P30, P40 and P50 failed under a compressive strain of about 30%. On the contrary, P10 and P20 endured more cycles at a strain of 60% without showing any damage, despite the presence of dissipative hysteresis loops resulting from viscoelasticity, with maximum values of 0.03 MPa at a strain



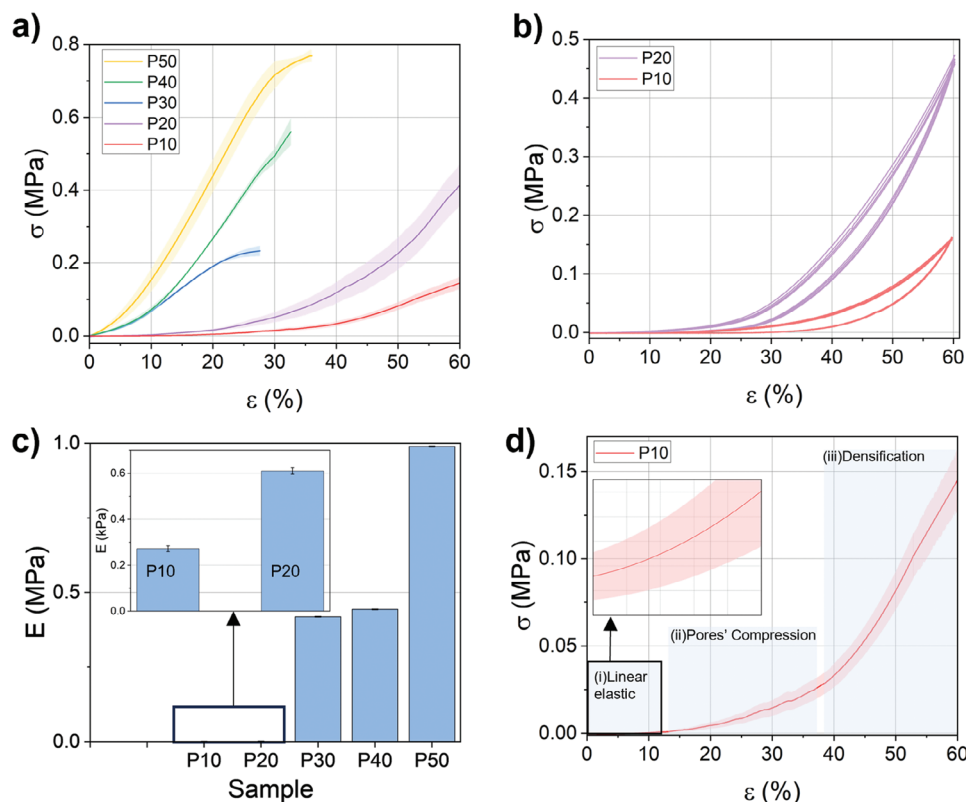


**Figure 4.** a) Compression stress-strain ( $\sigma$ - $\epsilon$ ) curves of cryogels with various amount of PEGDA, b) Cyclic tests for P10 and P20 cryogels c) Young Modulus  $E$  of the cryogels with various compositions, d) Stress-strain curve of P10 cryogels exhibiting the typical three deformation regimes of porous materials.

of 49.5 % for P10 and 0.058 MPa at a strain of 47.6 % for P20 (Figure 4b). The compressive modulus decreased with increasing PEGDA content, resulting in a softening of the tested cryogels, as reported in Figure 4c. The enhanced softness and deformability of P10 and P20 cryogels can be attributed to their higher porosity, which also influenced the shape of the stress-deformation curves. As highlighted in Figure 4d, these curves can be divided into three regimes: i) the linear elastic regime, where the Young's modulus is measured; ii) the collapse of pores, where compression serves to close the pores with minimal variation in stress; and iii) the densification regime, where the contact between the walls of closed pores increases the compressive resistance of the material.<sup>[56]</sup> Notably, P10 cryogels exhibited not only the lowest Young's Modulus ( $E$ ) but also the highest onset of densification, indicating that the larger pores in P10 cryogels were completely closed at higher compressive strains (around 40% deformation). After that point, the stress increased exponentially. The different mechanical and electrical properties that were obtained demonstrate the tailorable nature of the cryogel approach to meet desired requirements for 3D conductive structures, by simply adjusting the chemical composition of the initial hydrogel.

## 2.2. Optimization of the Material

To explore the potential of the proposed material approach for soft mechanical sensing, the P10 formulation was modified by incorporating a reactive diluent, specifically Lauryl Acrylate (LA). The

reactive diluent was expected to decrease the cross-linking density and, consequently, the stiffness of the material.<sup>[57]</sup> A surfactant (Polysorbate 20) was incorporated in the formulation to ensure a good miscibility of the hydrophobic monomers in the (PE-DOT:PSS)s/PEGDA solution. As shown in Figure S4a (Supporting Information), the reactive diluent did not alter the kinetics of the polymerization but reduced the cross-linking density, manifested in the lower final value of  $G'$  and confirmed by the nanoindentation tests performed on both solid and lyophilized samples (Figure S4b, Supporting Information). Compared to P10 samples, the size of the pores of P9.5\* was more than doubled, despite the slightly lower total porosity (Figure 5a,b), and the pores possessed a more oblong shape, as displayed in Figure 5c. Finally, the modified material had a lower Young Modulus and larger densification strain (Figure 5d,e), with the latter being caused by the larger pores. Figure 5f reports the effect of processing on the mechanical properties of P9.5\* samples. The freeze-drying did not affect the softness of the corresponding hydrogels but increased the maximum deformation strain. In particular, cryogels and hydrogels were tested by setting the maximum deformation at 60%. Under these conditions, three out of five hydrogels failed (at a deformation of  $51.4 \pm 1.8\%$ ), while all the cryogels withstood more cycles at the deformation of 60% without showing any damage (Figure S5a, Supporting Information). Moreover, freeze-drying not only preserved and improved the mechanical properties of the hydrogels but was necessary to stabilize the material. In fact, the printed hydrogels rapidly lost the water (see shrinkage at room temperature in Figure S5b, Supporting Information)

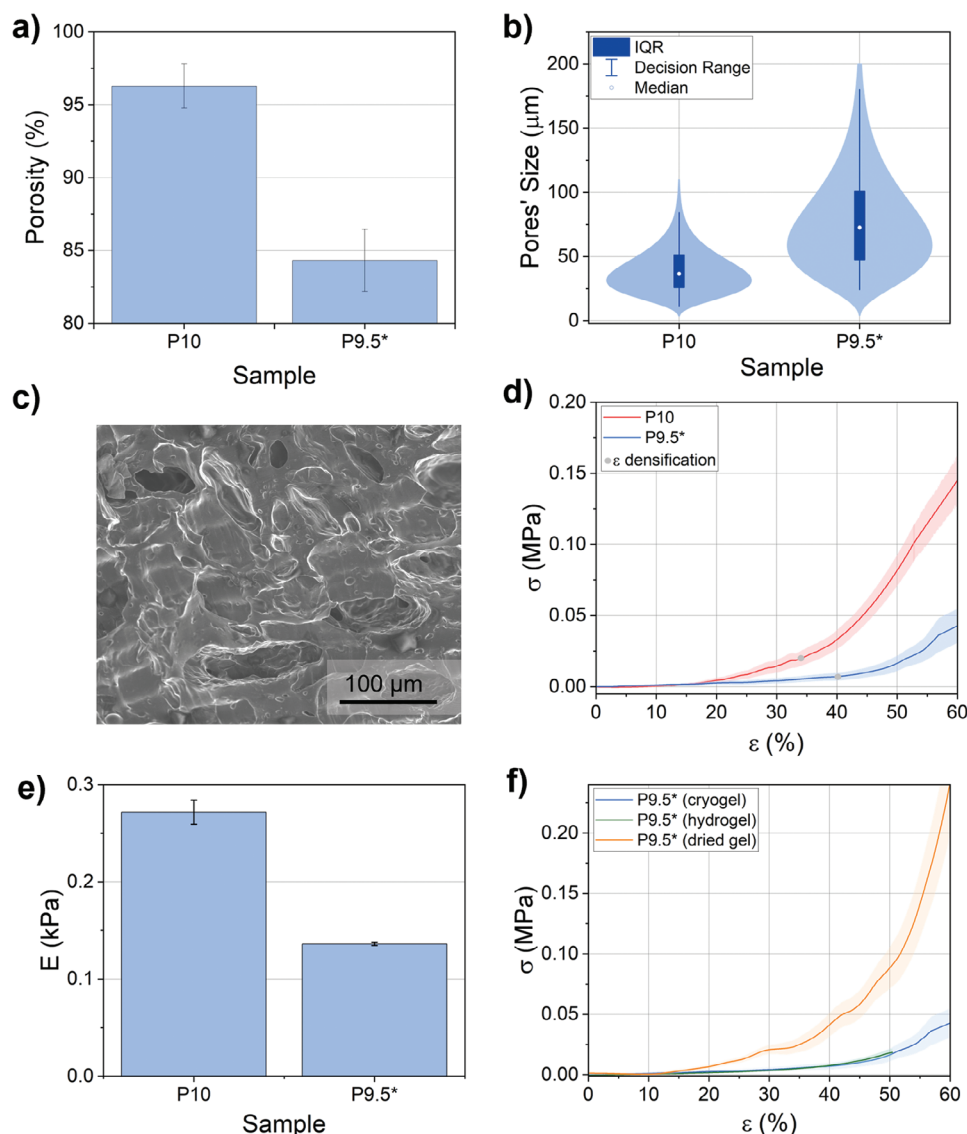


**Figure 5.** Properties of the optimized P9.5\* cryogels, including: a) The total porosity  $P$  respect to that of P10 cryogels; b) The violin plot distributions of the pores' size compared to that of P10 cryogels; c) SEM image of the pores of P9.5\* cryogels; d) The compression strain-stress ( $\sigma$ - $\epsilon$ ) curve of P9.5\* cryogels e) the Elastic Modulus  $E$  of the material compared to that of P10 samples; f) Comparison of the stress-strain curves of the P9.5\* cryogels, hydrogels and dried gels after 24 h of dehydration at room temperature and environmental pressure.

and became stiffer (Figure 5f). This could be related to the collapse of the pores during the evaporation of water at room conditions, as shown in the SEM images of the dried gels reported in Figure S5c,d (Supporting Information).

Lastly, the stability of the electrical properties of the P9.5\* cryogels under varying humidity levels was investigated due to the hydrophilic nature of the material (Table 1). At the high relative humidity of 90%, the resistance of the cryogel increased, likely due to the absorption of water molecules that made swell PSS shells, increasing the distances between adjacent PEDOT cores.<sup>[58]</sup> Nevertheless, the resistance was found to be stable up to 70% relative humidity, demonstrating the suitability of the material for applications in various environmental conditions.

### 2.3. 3D Printing

The printability of the P9.5\* formulation was tested by 3D printing simple shapes of different sizes. During the freeze-drying, the samples underwent a geometrical deformation due to the expansion of the solvent upon crystallization, which induced stresses from the external surface to the core of the samples,<sup>[59]</sup> and the external surface roughened after the extraction of the ice crystals. Nevertheless, the overall shape was maintained, and it was possible to obtain self-supporting 3D structures with fine features, as shown in Figure 6. Furthermore, the resulting cryogels experienced a volumetric shrinkage of 68% due to the water removal, which must be considered for the Computer-Aided

**Table 1.** Variation of the electrical resistance of P9.5\* cryogels at different levels of relative humidity.

Relative Humidity [%]	$R/R_0$			
	time: 0 h	time: 2 h	time: 6 h	time: 24 h
30	1	1	1	1
40	1	1	1	1
50	1	1	1	1
70	1	1	1	1
90	1	1.12	1.17	1.23

Design (CAD) (Figure S6h, Supporting Information). Nevertheless, the shrinkage allowed to further scale down the printed features and to obtain objects with microscopic resolution. In particular, even if the surface quality of the initial hydrogel resulted affected, the proposed method allowed to fabricate 60  $\mu\text{m}$ -thick walls, holes with a diameter of 370  $\mu\text{m}$  and circular pillars with a height and diameter equal to 125  $\mu\text{m}$  (Figure S6a-g, Supporting Information). Various parts were fabricated to demonstrate the versatility of the material and the process for different soft sensing applications, such as micro-structured electrodes (Figure 6a), conductive serpentine and wearable

sensing devices (Figure 6b). Noteworthy, despite the high water content, complex structures could be 3D-printed with good CAD fidelity, with a combination of conductive and insulating layers with good interface (Figure 6c), and at different sizes (Figure 6d,e), opening up more possibilities for multilayer and scalable sensors that can be tailored for different requirements.

## 2.4. Proof of Concept: Soft Force Sensors

To assess the suitability of the proposed material for fabricating resistive force sensors, 3D soft units were printed in a honeycomb (HC) configuration with hexagonal holes. This cellular topology notably reduces the mass density and increases the porosity with respect to the bulk material, while ensuring good mechanical strength.<sup>[60]</sup> Moreover, the unit cell is based on hexagonal geometries, with corners of 120°. This value overcomes the standard angle (45°) that is considered the minimum to fabricate overhanging structures.<sup>[61]</sup> As a result, overhanging cellular structures with walls as thin as 0.8 mm (0.5 mm after freeze-drying, as seen in Figure 6d) could be fabricated without adding any support. Additionally, a “bulk” sensor without cells was fabricated and analyzed as a reference. The design of the sensor is reported in Figure 7a. The volume of the sensor

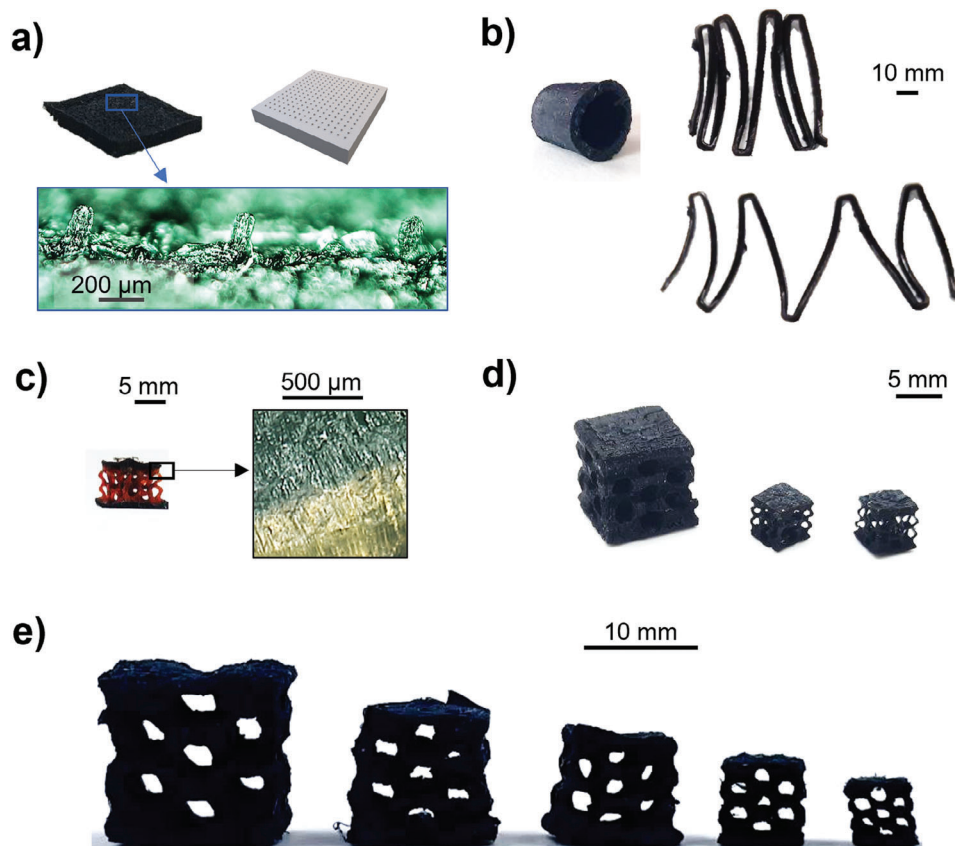


**Figure 6.** 3D printed cryogels from P9.5\* formulation. The potential applications of this material were showcased by printing different parts, such as: a) Structured 1.5 cm  $\times$  1.5 cm  $\times$  3 mm conductive electrode with an array of 15  $\times$  15 micro-sized pillars. The CAD model is reported as a reference. b) A hollow thimble for wearable applications, and conductive serpentine with variable length; c) Bi-material objects including a not conductive layer and the microscope image of the interface between the two materials, d) 3D complex geometries with an isotropic cellular morphology, e) that could be printed in different sizes.



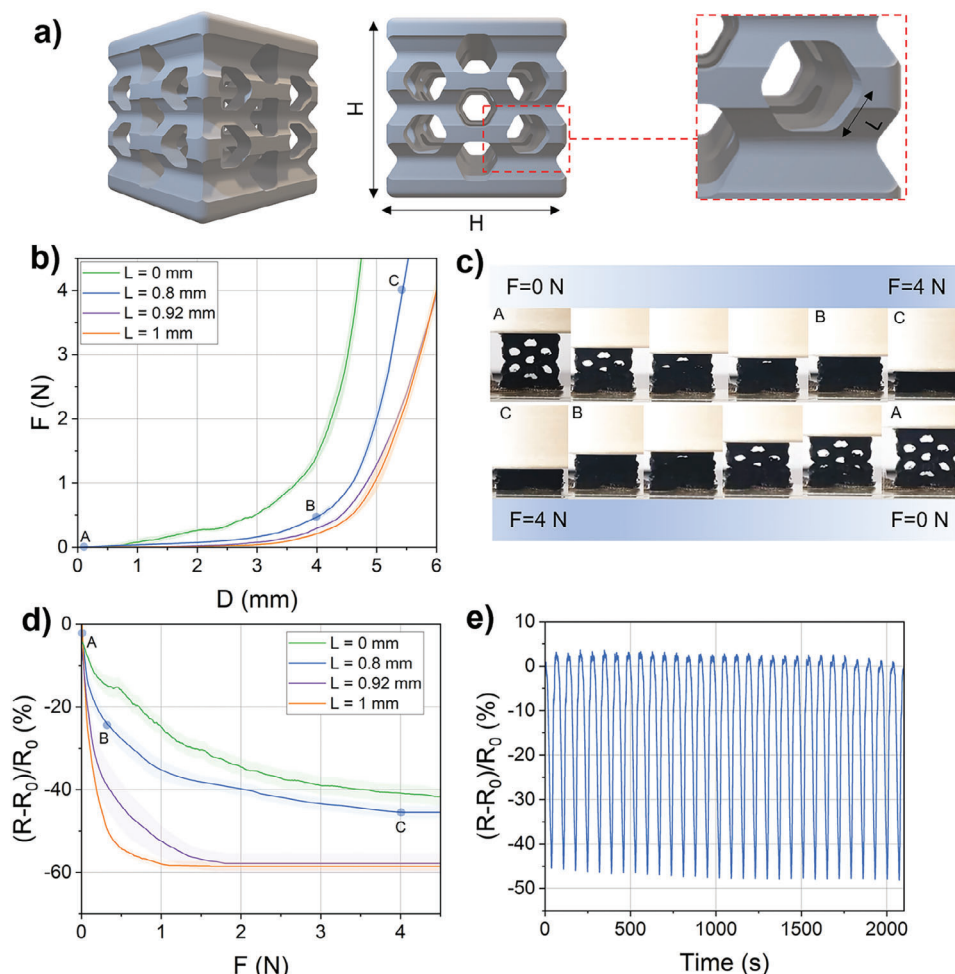


**Figure 7.** a) CAD model of the sensor. The height  $H$  of the sample, equal to its base, was kept constant. Four sensors were fabricated by setting the length  $L$  of the cells at 0 mm (bulk sensor), 0.8 mm, 0.92 mm and 1 mm. b) Displacement  $D$  versus Force  $F$  plots of the samples. The curve of case  $L = 0.8$  mm was used as a reference to identify the deformation steps during the loading phase: from A to B, the cells are smoothly closed, at C the material is compressed at a force of 4 N. c) Change in morphology during one cycle of loading-unloading of compression test. The variation of the electrical resistance of d) the sensors with different values of  $L$  at increasing force  $F$ , and of e) the  $L = 0.8$  mm sensor over time during the application of 30 consecutive loading-unloading compression cycles.

(i.e., the length  $H$ ) was kept constant, while the cells' size  $L$  was varied to study the impact of morphology on sensing performance. As depicted in Figure 7b, this approach allowed to custom the mechanical properties of the samples. In particular, the cells of the sensor architecture acted as additional porosity, delaying the onset of densification. The deformation mechanism in the HC parts was also influenced by the morphological distortion due to the freeze-drying step, with one surface of each sample assuming a slightly convex profile, as shown in Figure S7a (Supporting Information). This aspect, which occurred in a predictable and repeatable manner, affected the distribution of deformation compared to that of a perfectly symmetrical configuration (Figure S7b, Supporting Information). As reported in Figure 7c, the closure of the HC unit cells started from those at the bottom of the structure (i.e., those nearest to the convex surface), and proceeded toward the top within the densification regime. During the unloading phase, the opening of the cells occurred in the opposite direction, with the samples com-

pletely recovering their initial shape (Video S1, Supporting Information).

The electrical resistance of the cryogels was monitored during the application of the force in order to assess the suitability of the material to design force sensors. As shown in Figure 7d, the electrical resistance of both bulk and HC samples decreased upon compression, with the sensitivity trend depending on the 3D morphology. The electrical conductance of PEDOT:PSS and its polymer blends occurs via hopping of charge carriers.<sup>[62]</sup> Therefore, when the load was applied on the cryogels, both the compression of the sample, and the closure of the material micropores<sup>[63]</sup> and of the HC unit cells, reduced the distance between PEDOT oligomers and created new conducting paths, enhancing the possibility of carrier conduction. This resulted in the reduction of the electrical resistance that, for the bulk sensors, dropped down to 45% of its initial value. In the soft sensors, the change in resistance was influenced by the different deformation behavior produced by the presence of the HC unit cells. The trend

**Table 2.** Sensitivity of the 3D-printed sensors with different cells' size  $L$ .

$L$ [mm]	Stress Range [kPa]	Sensitivity [kPa <sup>-1</sup> ]
0	0 – 6	2
	6 – 25	0.96
	25 – 50	0.35
	50 – 80	0.1
0.8	0 – 6	2.9
	6 – 15	1.4
	15 – 80	0.13
0.92	0 – 4	11.7
	4 – 8	1.8
	8 – 25	1.06
1	0 – 1.5	20
	1.5 – 5	6
	5 – 8	1.7
	5 – 15	0.44

was similar for each sensor, since the deformation mechanism in hierarchical structures is ruled by the cell's shape rather than their size.<sup>[64]</sup> The larger densification phase during compression corresponded to the abrupt collapsing of the electrical resistance at lower forces, followed by a smoother reduction until the threshold for the signal saturation. The latter was lower than that of bulk sensors due to the inferior stiffness of the samples.

Overall, adding the hexagonal cells reduced the range of force detection but, reversely, enhanced the variation of resistance at lower forces. These two effects became more prominent by increasing the size  $L$ , with the sensor possessing larger cells exhibiting a halving in the resistance at merely 0.2N, but a saturation threshold of 1N. The maximum sensitivity for each sensor is reported in Table 2. The sensors possessing  $L$  equal to 1 mm exhibited a notable sensitivity of 20 kPa<sup>-1</sup> in the range of 0 – 1.5 kPa, which is larger than that of other 3D-printed soft sensors working in low-stress range.<sup>[65,66]</sup> Nevertheless, among the HC sensors, the one with  $L = 0.8$  mm had the best compromise between sensitivity, linearity, and working range, showing a sensitivity of 2.9 kPa<sup>-1</sup> up to 6 kPa, 1.4 kPa<sup>-1</sup> in the range of 6 – 15 kPa and 0.13 kPa<sup>-1</sup> in the range of 15 kPa – 80 kPa. Up to 80 kPa, these results are larger than those reported for other 3D-printed porous sensors.<sup>[67–69]</sup> Moreover, the sensor with  $L$  equal to 0.8 mm showed a good signal stability over time (Figure 7e). These results demonstrated the potential of the proposed material to tune the sensor's properties depending on the 3D printed morphology. Definitely, the great opportunities of DLP in terms of design offer the possibility to further improve the sensing performance and to develop optimized designs for tactile sensors that can meet diverse requirements.

### 3. Conclusion

In this paper, we presented a novel fabrication method involving cryogelation and DLP 3D printing to create 3D-printable materials for soft sensing. The combination of the two processes offers a versatile approach to tailor the mechanical and electrical properties of complex structures, making them suitable for a wide range

of applications in soft robotics. The use of DLP 3D printing enabled the creation of soft conductive structures with excellent resolution, shape fidelity, and fine details. The cryogelation process effectively removed the liquid phase from the hydrogels, resulting in the fabrication of microporous cryogels. Additionally, the porosity and the mechanical properties could be adjusted by controlling the chemical composition, providing the means to tailor the soft sensor's response to compressive forces. In particular, cryogels with higher PEGDA content demonstrated an increased stiffness and density, while those with lower PEGDA concentration exhibited enhanced deformability and higher porosity, and the addition of a reactive diluent further enhanced the material's deformability and allowed for the fabrication of larger pores. Furthermore, this approach proved to be versatile, allowing the fabrication of various intricate 3D structures with high resolution and shape fidelity. The cryogelation process effectively maintained the details of the 3D-printed structures, enabling the creation of soft sensors with microstructures and complex geometries that influenced the sensing behavior. In conclusion, the versatility of the material and fabrication method opens up opportunities for various soft sensing applications, and the ability to customize the material's properties allows for tailoring the sensors to meet specific requirements. We had earlier demonstrated the approach of harnessing both micropores and a lattice design (macropores) to enhance the deformation for soft actuation<sup>[70,71]</sup> by printing polymerizable emulsions. In this regard, the possibility of fabricating multimaterial 3D cryogels can offer interesting opportunities for future investigation of sensorized actuators with programmed morphologies, and that can be 3D-printed all-in-one. Moreover, the combination of 3D printing and cryogelation can be extended to other materials, expanding the potential of this fabrication approach for the development of soft sensors with diverse functionalities.

### 4. Experimental Section

**Materials:** Poly(ethylene glycol) diacrylate (PEGDA) (molecular weight 700), Reactive Orange 16, Lithium phenyl-2,4,6-trimethylbenzoylphosphine (LAP), Polysorbate 20 (PS20), and Lauryl Acrylate (LA) were purchased from Sigma-Aldrich (St. Louis, Missouri, US). Poly(3,4-ethylenedioxythiophene) Polystyrene sulfonate (PEDOT:PSS) was purchased from Heraeus (Hanau, DE) in form of an aqueous solution (Clevios™ PH 1000). Silver conductive glue was purchased from MG Chemicals (MG Chemicals, Burlington, CA).

**Methods:** The next sections encompass the procedure to prepare and characterize the formulations, the cryogels and the force sensors. Photosensitivity and Electrical Formulations Analysis illustrates the methods to investigate the formulations and the hydrogels in terms of optical, rheological and electrical properties, and printability. The mechanical characterization of the cryogels and the optimization of the material for soft sensing is reported in Fabrication and Characterization of the cryogels. Finally, Design, Fabrication and Characterization of the Sensors describes the fabrication and characterization of the 3D force sensors.

**Photosensitivity and Electrical Formulations Analysis:** To study the effect of the composition on the photosensitive formulations, the amount of PEGDA was increased from 10 to 50 wt% and the amount of the photoinitiator was fixed at 0.5 phr respect to PEGDA. The amount of (PEDOT:PSS)s varied accordingly. The chemicals were mixed at room temperature under magnetic stirring to obtain homogeneous solutions. The viscoelastic properties of the formulations were evaluated using a rheometer (Physica MCR 302, Anton Paar, Graz, AUT) in a 25 mm parallel

**Table 3.** Chemical formulations of the hydrogels' precursors of the 3D cryogels.

Formulation	PEGDA [wt%]	EG/(PEDOT : PSS)s [%]	LA [wt%]	polysorbate [wt%]
P50	50	8	0	0
P30	30	8	0	0
P20	20	8	0	0
P10	10	8	0	0
P9.5*	9.5	8	0.9	4.7
Insulating cryogel	15	0	0	0

a) the content of LAP was fixed at 0.5 phr (respect to PEGDA) for each formulation.

plate mode. The gap between the plates was fixed at 0.3 mm for each experiment. The shear rate was increased from 0 to  $100 \text{ s}^{-1}$  to measure the viscosity. Amplitude sweep tests were performed increasing the amplitude strain from 0.01% to 100% while keeping the frequency at 1 Hz. For the real-time photorheological tests, the instrument was equipped with a quartz bottom plate and a UV-light source (Hamamatsu LC8 lamp, Hamamatsu Photonics, Shizuoka, JPN). The light intensity was fixed at  $12 \text{ mW cm}^{-2}$ . The lamp was switched on after 60 s to allow the system to stabilize before the onset of polymerization. Time sweep measurements were performed during irradiation at a constant frequency of 1 Hz and within the linear viscoelastic region (strain amplitude of 0.1%). Furthermore, Absorbance UV-vis spectra were collected using a multimode reader (Synergy HTX, BioTek, Winooski, US) in the range between 350 and 650 nm and at a scan rate of  $1 \text{ nm min}^{-1}$ .

The amount of (PEDOT:PSS)s respect to the total formulation was increased from 5 to 90 wt% PEGDA, (PEDOT:PSS)s to study the effect of PEDOT:PSS loading on the electrical activity, and LAP (0.5 phr respect to PEGDA) were mixed under magnetic stirring at room temperature. The action of EG was examined by fixing the amount of PEGDA at 10 wt% and varying the ratio EG/(PEDOT : PSS)s (0.05, 0.08 and 0.2). PEDOT:PSS and EG were mixed at  $90^\circ\text{C}$  for 2 h before adding PEGDA and LAP. For each composition, thin samples were 3D-printed, freeze-dried and wired. The resistance was acquired through a Digital Multimeter (34460A, Keysight, Santa Rosa, US). The resistivity  $\rho$  was calculated according to the 2nd Ohm's law. Thermal analysis (TGA Model Q500, TA Instrument, New Castle, DE) was used to analyze the thermal stability of the P10 cryogels containing EG. ThermoGravimetric Analysis (TGA) and Differential Thermal Analysis (DTA) were carried out to assess the presence of EG after the lyophilization. The tests were performed under a nitrogen atmosphere by keeping the flow rate of  $50 \text{ mL min}^{-1}$ . A first step at  $30^\circ\text{C}$  was used to stabilize the samples before increasing the temperature from 30 to  $800^\circ\text{C}$  at a scanning rate of  $10^\circ\text{C min}^{-1}$ .

**3D Printing:** An Asiga DLP 3D printer (Asiga, Alexandria, AUS) with a light source of 385 nm and a xy resolution of  $62 \mu\text{m}$  was used to 3D print the formulations. The photoreactivity of the formulation with different amount of PEGDA was studied by using the Material Test feature of the printer. A small drop of formulation was deposited on the build tray, on which a circular spot (diameter  $\varnothing = 6 \text{ mm}$ ) was irradiated for a controlled time until the formulation cured. For printing, the CAD models were converted into .stl files and sent to the 3D printer. The layer thickness and the light intensity were set as  $50 \mu\text{m}$  and  $12 \text{ mW cm}^{-2}$ , respectively, while the exposure time for layer was adjusted according to the printed formulation. 3D printed parts were post-cured under UV light for 3 min under an ultraviolet Flash unit (Asiga, Alexandria, AUS).

**Fabrication and Characterization of the Cryogels:** The precursors hydrogels of the cryogels were 3D printed by varying the amount of PEGDA. The chemical compositions are reported in Table 3. P50, P40, P30, P20, and P10 formulations were prepared as described in Photosensitivity and Electrical Formulations Analysis. For P9.5\* samples, Polysorbate 20 (PS20) was mixed with PEGDA, (PEDOT:PSS)s, EG and LAP for 30 min before adding LA. In the insulating hydrogel, (PEDOT:PSS)s was replaced with

distilled water, and a dye (Reactive Orange 16) was used to improve the printing resolution.

The 3D printed hydrogels were immersed in distilled water for 24 h, frozen at  $-80^\circ\text{C}$  and freeze-dried for 24 h through a LIO-5P 4K lyophilizer (Levanchimica Srl, Bari, IT). The swelling of the cryogels was determined by immersing the samples in distilled water for 24 h. Thereafter, the cryogels were removed from the water and carefully dried with paper. Given the hydrogels' initial and final weight  $W_0$  and  $W_f$ , the Swelling Degree (SD) can be calculated as:

$$SD = \frac{(W_f - W_0) * 100}{W_0} \quad (1)$$

The Porosity (P) of cryogels was measured succeeding overnight immersion in absolute ethanol according to the following equation:

$$P = \frac{(W_f - W_0)}{d * V} \quad (2)$$

where  $d$  is the density of the ethanol and  $V$  is the final volume of the cryogels.

The lyophilized samples were frozen and sectioned to investigate their morphology.

Scanning Electron Microscope (SEM) images were collected through a Zeiss EVO LS10 (Carl Zeiss AG, Oberkochen, DE). The accelerating voltage and the working distance were set at 5 kV and at 10 mm, respectively. The cryogels were frozen at  $-80^\circ\text{C}$  and cut along the z-direction (referring to the direction of freeze-drying) in order to examine the cross-section of the samples. The obtained images were analyzed using ImageJ software to calculate the size of the pores as the maximum Feret diameter. For each sample, 50 pores were measured. Different distributions (Lognormal, Weibull, Exponential and Gamma) were compared to the collected data; the goodness of fit was evaluated by considering the p-value of the modified Kolmogorov-Smirnov test (OriginLab Corporation, Northampton, US). For the violin plots, the statistical dispersion was measured with the Interquartile Range IQR. To detect the outliers, the lower bound (Q1) and upper bound (Q3) of the decision range were calculated as  $Q1 + (1.5 * IQR)$  and  $Q3 - (1.5 * IQR)$ , respectively. The interface between conductive and dielectric cryogels in bi-material components, as well as the features of printed samples, was observed by using a digital microscope (Hirox, Tokyo, JP). The shrinkage of cryogels and dried gels was measured as:

$$Shrinkage = 100 * \frac{(V - V_0)}{V_0} \quad (3)$$

in which  $V$  and  $V_0$  are the final and initial volume of the samples. The mechanical properties of cryogels ( $10 \text{ mm} \times 10 \text{ mm} \times 10 \text{ mm}$ ) were tested using ad hoc compression set-up. The sample was fixed using a bi-adhesive tape to a glass put on a Lab Jack (Newport 271, MKS Instruments, Inc.), which was positioned under a force platform. The latter consisted of one orthogonal manual micrometric translation stage (M-105.10, Physik Instrumente, Karlsruhe, Germany) coupled with a micrometric servo-controlled translation stage (M-111.1DG, Physik Instrumente, Karlsruhe, Germany) (for a precision vertical positioning). A Delrin probe was mechanically interfaced to the previous translation stage and to a triaxial load cell (ATI Nano 17, ATI Industrial Automation, Inc., Apex, NC, USA). The probe exerted a vertical force on the sample beneath it. Each acquisition starts by bringing the stage to the highest vertical position, while the hardware peripherals are initialized. Compression cyclic tests were performed at a speed rate of  $0.1 \text{ mm s}^{-1}$ . For each sample, five cycles were performed at a maximum deformation of 60%. To evaluate the effect of freeze-drying on the material, P9.5\* hydrogels were printed and immediately tested as just described to assess the mechanical properties. The same experiments were carried out on dried gels that were obtained by dehydrating the hydrogels at environmental pressure and room temperature for 24 h. Dynamic nanoindentation experiments were performed on P9.5\* and P10 cryogels through an iNano indentation system (Nanomechanics, Inc., San Jose, CA), using a nanoindenter a flat-punch tip with a diameter of  $109 \mu\text{m}$ . The

frequency was varied from 1 to 200 Hz. In order to determine the achievable resolution of P9.5\* formulations, an array containing holes, walls, and pillars with circular section were 3D printed and lyophilized. The diameter of both pillars and holes, and the thickness of the walls, was varied from 1 to 0.1 mm. Cubic samples of P9.5\* cryogels were wired to observe the dependence of the electrical resistance of the material to humidity. The tests were performed using a Climatic Test Chamber (CTC256, Memmert GmbH, Schwabach, DE). The temperature was set at 25 °C while the Relative Humidity (RH) was step-wise increased from 10% to 90%. Each RH step was held for different time intervals up to 24 h.

**Design, Fabrication and Characterization of the Sensors:** The 3D structure was initially designed with SolidWorks (Dassault Systèmes, Waltham, US) and then simulated through a parametric study to identify parameters to adjust the deformation under a prescribed normal load. The simulation was conducted on COMSOL Multiphysics 5.6 (COMSOL AB, Stockholm, Sweden) under steady-state assumption, simulating the material with a nonlinear viscoelastic model. A fixed constraint was imposed on the sensor's base, while a distributed normal load was applied to the top surface. Finally, the (L) of the honeycomb cells was modified to simulate the mechanical behavior of morphologies with different densities and void fractions under a prescribed load in the range 0 to 5 N. Four values of (L) were selected, and the respective cylindrical and honeycomb structures were 3D printed with P9.5\* hydrogels to test mechano-sensing behavior. The hydrogels were lyophilized to obtain cryogels according to the procedure reported in Fabrication and Characterization of the Cryogels. Strips of conductive tissues were bonded to the sensor through silver paste, keeping the samples at 65 °C for 15 min. The cyclic compression tests were conducted with the same platform described in Fabrication and Characterization of the Cryogels at a speed of 0.1 mm s<sup>-1</sup> and at a sampling rate of 100 Hz. The displacement was fixed at a 4.5 mm, and the electrical resistance was recorded. Given the resistance of the sensor before and during the test ( $R_0$  and  $R_s$ ), and the applied compressive stress  $\sigma$ , the sensor's sensitivity was calculated:

$$\text{sensitivity} = \frac{1}{\sigma} \frac{(R_s - R_0)}{R_0} \quad (4)$$

## Supporting Information

Supporting Information is available from the Wiley Online Library or from the author.

## Acknowledgements

This work was partially funded by the European Union's Horizon 2020 research and innovation programme under grant agreement No. 101069536 (MOZART project).

## Conflict of Interest

The authors declare no conflict of interest.

## Data Availability Statement

The data that support the findings of this study are available from the corresponding author upon reasonable request.

## Keywords

conductive cryogels, DLP (Digital Light Processing) 3D printing, photopolymerization, porous materials, soft sensors

Received: December 20, 2023  
Published online:

- [1] H. Wang, M. Totaro, L. Beccai, *Adv. Sci.* **2018**, *5*, 1800541.
- [2] G. D. Goh, G. L. Goh, Z. Lyu, M. Z. Ariffin, W. Y. Yeong, G. Z. Lum, D. Campolo, B. S. Han, H. Y. A. Wong, *Adv. Mater. Technol.* **2022**, *7*, 2101672.
- [3] A. Golgouneh, L. E. Dunne, *IEEE Rev. Biomed. Eng.* **2022**, *17*, 166.
- [4] F. Pujol-Vila, P. Güell-Grau, J. Nogués, M. Alvarez, B. Sepúlveda, *Adv. Funct. Mater.* **2023**, *33*, 2213109.
- [5] Y. Song, N. Wang, C. Hu, Z. L. Wang, Y. Yang, *Nano Energy* **2021**, *84*, 105919.
- [6] D. Cafiso, S. Lantean, C. F. Pirri, L. Beccai, *Adv. Intell. Syst.* **2023**, *5*, 2200373.
- [7] S. Mousavi, D. Howard, F. Zhang, J. Leng, C. H. Wang, *ACS Appl. Mater. Interfaces* **2020**, *12*, 15631.
- [8] J. Qin, L. J. Yin, Y. N. Hao, S. L. Zhong, D. L. Zhang, K. Bi, Y. X. Zhang, Y. Zhao, Z. M. Dang, *Adv. Mater.* **2021**, *33*, 2008267.
- [9] J. Qu, Q. Wu, T. Clancy, Q. Fan, X. Wang, X. Liu, *IEEE Sens. J.* **2020**, *20*, 6971.
- [10] B. Shih, C. Christianson, K. Gillespie, S. Lee, J. Mayeda, Z. Huo, M. T. Tolley, *Front. Robot. AI* **2019**, *6*, 1.
- [11] S. Miralles-Comins, M. Zanatta, V. Sans, *Polymers* **2022**, *14*, 5121.
- [12] X. Y. Yin, Y. Zhang, J. Xiao, C. Moorlag, J. Yang, *Adv. Funct. Mater.* **2019**, *29*, 1904716.
- [13] L. Zhu, Y. Rong, Y. Wang, Q. Bao, J. An, D. Huang, X. Huang, *Eur. Polym. J.* **2023**, *187*, 111886.
- [14] D. Cafiso, A. A. Septevani, C. Noè, T. Schiller, C. F. Pirri, I. Roppolo, A. Chiappone, *Sustainable Mater. Technol.* **2022**, *32*, 2205326.
- [15] Y. Yang, K. Shi, K. Yu, F. Xing, H. Lai, Y. Zhou, P. Xiao, *Adv. Healthcare Mater.* **2022**, *11*, 2101504.
- [16] X. Jing, H. Li, H.-Y. Mi, Y.-J. Liu, P.-Y. Feng, Y.-M. Tan, L.-S. Turng, *Sens. Actuators B: Chem.* **2019**, *295*, 156.
- [17] X. Yu, H. Z. Y. W. X. Fan, Z. Li, X. Zhang, T. Liu, *Adv. Funct. Mater.* **2022**, *32*, 2204366.
- [18] G. Mogli, A. Chiappone, A. Sacco, C. F. Pirri, S. Stassi, *ACS Appl. Electron. Mater.* **2023**, *5*, 108324.
- [19] Y. Li, D. Yang, Z. Wu, F.-L. Gao, X.-Z. Gao, H.-Y. Zhao, X. Li, Z.-Z. Yu, *Nano Energy* **2023**, *109*, 108324.
- [20] L. Hu, P. L. Chee, S. Sugianto, Y. Yu, C. Shi, R. Yan, Z. Yao, X. Shi, J. Zhi, D. Kai, H.-D. Yu, W. Huang, *Adv. Mater.* **2022**, *35*, 2205326.
- [21] S. Bashir, M. Hina, J. Iqbal, A. H. Rajpar, M. A. Mujtaba, N. A. Alghamdi, S. Wageh, K. Ramesh, S. Ramesh, *Polymers* **2020**, *12*, 1.
- [22] Z. Guo, C. Ma, W. Xie, A. Tang, W. Liu, *Carbohydr. Polym.* **2023**, *315*, 121006.
- [23] C. Lin, H. Y. Yang, *Mater. Today: Proc.* **2022**, *70*, 265.
- [24] X. Y. Yin, Y. Zhang, X. Cai, Q. Guo, J. Yang, Z. L. Wang, *Mater. Horiz.* **2019**, *6*, 767.
- [25] H. Zhu, X. Hu, B. Liu, Z. Chen, S. Qu, *ACS Appl. Mater. Interfaces* **2021**, *13*, 59243.
- [26] M. A. Bhat, R. A. Rather, A. H. Shalla, *Synth. Met.* **2021**, *273*, 116709.
- [27] Y. Lee, W. Song, J.-Y. Sun, *Mater. Today Phys.* **2020**, *15*, 100258.
- [28] M. Abshirini, M. C. Saha, M. C. Altan, Y. Liu, *Adv. Mater. Technol.* **2022**, *7*, 2101555.
- [29] Q. Chen, P. F. Cao, R. C. Advincula, *Adv. Funct. Mater.* **2018**, *28*, 1800631.
- [30] L. Yang, R. Wang, Q. Song, Y. Liu, Q. Zhao, Y. Shen, *Compos. Part A: Appl. Sci. Manuf.* **2017**, *101*, 195.
- [31] Z. Zheng, Y. Zhao, Z. Ye, J. Hu, H. Wang, *J. Colloid Interface Sci.* **2022**, *618*, 290.
- [32] S. Peng, S. Wu, Y. Yu, B. Xia, N. H. Lovell, C. H. Wang, *ACS Appl. Mater. Interfaces* **2020**, *12*, 22179.
- [33] H. Cui, Y. Liu, R. Tang, J. Ren, L. Yao, Y. Cai, D. Chen, *Micromachines* **2023**, *14*, 662.
- [34] Y. Jiang, Z. Xu, T. Huang, Y. Liu, F. Guo, J. Xi, W. Gao, C. Gao, *Adv. Funct. Mater.* **2018**, *28*, 1707024.



- [35] Q. Chen, J. Shen, D. Estevez, Y. Chen, Z. Zhu, J. Yin, F. Qin, *Adv. Funct. Mater.* **2023**, 2302545.
- [36] H. Francon, Z. Wang, A. Marais, K. Mystek, A. Piper, H. Granberg, A. Malti, P. Gatenholm, P. A. Larsson, L. Wagberg, *Adv. Funct. Mater.* **2020**, 30, 2200373.
- [37] B. An, Y. Ma, W. Li, M. Su, F. Li, Y. Song, *Chem. Commun.* **2016**, 52, 10948.
- [38] B. Wang, M. Gao, X. Fu, M. Geng, Y. Liu, N. Cheng, J. Li, L. Li, Z. Zhang, Y. Song, *Nano Energy* **2023**, 107, 108135.
- [39] J. Li, C. Boyer, X. Zhang, *Macromol. Mater. Eng.* **2022**, 307, 2200010.
- [40] X. Mo, L. Ouyang, Z. Xiong, T. Zhang, *Biomed. Mater. (Bristol)* **2022**, 17, 042002.
- [41] J. R. Choi, K. W. Yong, J. Y. Choi, A. C. Cowie, *BioTechniques* **2019**, 66, 40.
- [42] W. W. Tetsuro Majima, Wolfram Schnabel, *Macromol. Chem. Phys.* **1991**, 192, 2307.
- [43] Y. Yao, N. Sha, Z. Zhao, *Conf. Series: Mater. Sci. Eng.* **2019**, 678, 012016.
- [44] X. Fan, W. Nie, H. Tsai, N. Wang, H. Huang, Y. Cheng, R. Wen, L. Ma, F. Yan, Y. Xia, *Adv. Sci.* **2019**, 6, 1900813.
- [45] S. Khasim, A. Pasha, M. Lakshmi, P. Chellasamy, M. Kadarkarai, A. A. Darwish, T. A. Hamdalla, S. A. Al-Ghamdi, S. Alfidhli, *Opt. Mater.* **2022**, 125, 112109.
- [46] S. Y. Lien, P. C. Lin, W. R. Chen, C. H. Liu, P. W. Sze, N. F. Wang, C. J. Huang, *Crystals* **2022**, 12, 57.
- [47] S. Tu, T. Tian, A. L. Oechsle, S. Yin, X. Jiang, W. Cao, N. Li, M. A. Scheel, L. K. Reb, S. Hou, A. S. Bandarenka, M. Schwartzkopf, S. V. Roth, P. Müller-Buschbaum, *Chem. Eng. J.* **2022**, 429, 132295.
- [48] A. Srivastava, R. K. Sharma, D. Sharma, J. S. Tawale, V. V. Agrawal, S. K. Srivastava, *Opt. Mater.* **2022**, 134, 112922.
- [49] N. Lopez-Larrea, M. Criado-Gonzalez, A. Dominguez-Alfaro, N. Alegret, I. D. Agua, B. Marchiori, D. Mecerreyes, *ACS Appl. Polym. Mater.* **2022**, 4, 6749.
- [50] H. Peng, Y. Wang, *Appl. Phys. A* **2016**, 122, 516.
- [51] P. Jia, X. Wang, *J. Porous Mater.* **2022**, 29, 745.
- [52] J. P. Vareda, A. Lamy-Mendes, L. Durães, *Microporous Mesoporous Mater.* **2018**, 258, 211.
- [53] M. Guastaferro, L. Baldino, E. Reverchon, S. Cardea, *Gels (Basel, Switzerland)* **2021**, 7, 198.
- [54] F. D. Latief, *J. Phys.: Conf. Ser.* **2016**, 739, 012047.
- [55] Z. T. Mazraeh-shahi, A. M. Shoushtari, A. R. Bahramian, M. Abdouss, *J. Ind. Eng. Chem.* **2015**, 21, 797.
- [56] A. Rege, *Materials* **2021**, 14, 2731.
- [57] S. Lantean, G. Barrera, C. F. Pirri, P. Tiberto, M. Sangermano, I. Roppolo, G. Rizza, *Adv. Mater. Technol.* **2019**, 4, 2725.
- [58] A. L. Oechsle, T. S. L. Deville, T. Xiao, T. Tian, A. Vagias, S. Bernstorff, P. Müller-Buschbaum, *ACS Appl. Mater. Interfaces* **2023**, 15, 47682.
- [59] C. García-González, M. Camino-Rey, M. Alnaief, C. Zetzl, I. Smirnova, *J. Supercrit. Fluids* **2012**, 66, 297.
- [60] C. Qi, F. Jiang, S. Yang, *Compos. Part B: Eng.* **2021**, 227, 109393.
- [61] A. Garaigordobil, R. Ansola, E. Veguería, I. Fernandez, *Computer-Aided Design* **2019**, 109, 33.
- [62] A. M. Nardes, M. Kemerink, R. A. J. Janssen, J. A. M. Bastiaansen, N. M. M. Kiggen, B. M. W. Langeveld, A. J. J. M. van Breemen, M. M. de Kok, *Adv. Mater.* **2007**, 19, 1196.
- [63] T. Zhao, T. Li, L. Chen, L. Yuan, X. Li, J. Zhang, *ACS Appl. Mater. Interfaces* **2019**, 11, 29466.
- [64] E. Davoodi, H. Montazerian, R. Haghniaz, A. Rashidi, S. Ahadian, A. Sheikhi, J. Chen, A. Khademhosseini, A. S. Milani, M. Hoorfar, E. Toyserkani, *ACS Nano* **2020**, 14, 1520.
- [65] W. Yang, Y. Liu, W. Xu, H. Y. Niek, *Adv. Mater.* **2021**, 21, 10473.
- [66] Z. Tang, S. Jia, C. Zhou, B. Li, *ACS Appl. Mater. Interfaces* **2020**, 12, 28669.
- [67] M. Fortunato, L. Pacitto, N. Pesce, A. Tamburrano, *Sensors* **2023**, 23, 2300367.
- [68] X. Karagiorgis, G. Khandelwal, A. Beniwal, R. Chirila, P. J. Skabara, R. Dahiya, *Adv. Intell. Syst.* **2023**, 2300367.
- [69] M. Alsharari, B. Chen, W. Shuno, *Adv. Electron. Mater.* **2021**, 8, 2100597.
- [70] S. Joe, O. Bliah, S. Magdassi, L. Beccai, *Adv. Sci.* **2023**, 10, 2302080.
- [71] O. Bliah, S. Joe, R. Reinberg, A. B. Nardin, L. Beccai, S. Magdassi, *Mater. Horiz.* **2023**, 10, 4976.